Computational Methods in Applied Mathematics
Ahead of Print, pp. 1–25

Doi: 10.1515/cmam-2014-0003

DE GRUYTER

Central-Upwind Scheme for Savage–Hutter Type Model of Submarine Landslides and Generated Tsunami Waves

Alexander Kurganov · Jason Miller

Abstract — We develop a new central-upwind scheme for a one-dimensional Savage–Hutter type model of submarine landslides and generated tsunami waves. Our scheme exactly preserves physically relevant steady-states, preserves positivity of water depth, is insensitive to choice of discretization of nonconservative products, and properly incorporates friction inherent in the model. We apply our scheme to a variety of test problems and the numerical results clearly demonstrate a high accuracy and robustness of the proposed method.

2010 Mathematical subject classification: 76M12, 65M08, 86-08, 86A05, 35L65.

Keywords: Hyperbolic Systems of Balance Laws, Godunov-Type Central-Upwind Schemes, Well-Balanced Schemes, Nonconservative Products.

1. Introduction

It is well known that tsunamis can form when earthquakes below the ocean cause landslides on the ocean floor (see, e.g., [19, 32] and references therein). When in deep water, tsunamis have a height of only around 30 cm, but have a very long wave length. These waves, however, can be disastrous when they reach the shore. They contain an immense amount of energy, and when the water becomes shallower they slow down and increase in height (a process called wave shoaling). The size, speed, and shape of the wave as it comes ashore can all impact how the wave behaves once it reaches the shoreline, so it is important to have accurate models that can depict the true mechanisms by which tsunamis form.

Many existing tsunami models use the prescribed motion of a submerged rigid object to generate waves at the water surface. The motion of this object is determined by ODEs for the center of mass, which can be solved independently of the system describing the water motion (see, e.g., [13, 17, 34, 35]). These situations can be modeled by the Saint-Venant system with time-dependent bottom topography (see, e.g., [24]). Results from this model mimic analogous laboratory experiments in which a submerged solid object slides along the bottom of the water body, such as those found in [18]. In the real world, the mass sliding on the ocean floor also deforms and its deformation may substantially affect generated surface waves.

Alexander Kurganov
Mathematics Department, Tulane University, 6823 St. Charles Ave., New Orleans, LA 70118, USA
E-mail: `kurganov@math.tulane.edu`.

Jason Miller
Mathematics Department, Tulane University, 6823 St. Charles Ave., New Orleans, LA 70118, USA
E-mail: `jmiller8@tulane.edu`.

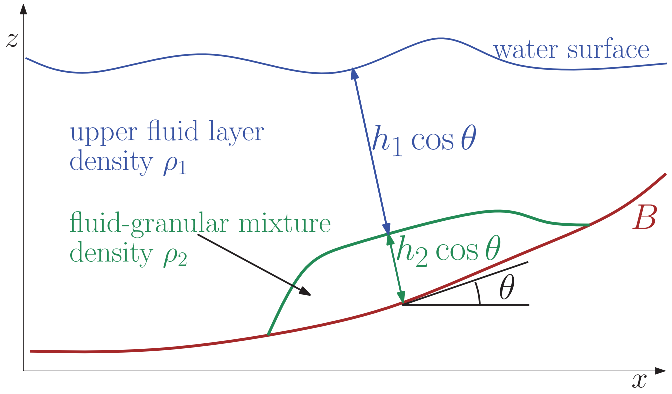

Figure 1. Diagram depicting the physical setting for the model. The fluid-granular layer with density ρ_2 and depth h_2 sits atop a non-erodible bottom B. A fluid layer with density ρ_1 sits atop the lower layer and the bottom.

The model studied here is a one-dimensional (1-D) Savage–Hutter type model for submarine avalanches and generated tsunami which was presented in [14], and is an improvement of an earlier model proposed by [19]. In this model, the sliding object is considered to be a fluid-granular mixture, which deforms as it slides down a solid bottom. This results a two-layer model where the upper layer is water and the lower layer is a fluid-granular mixture. The flow of the lower layer is driven by gravity and the interaction with the bottom of the water body while it also deforms due to momentum exchange with the upper fluid layer. This leads to a more realistic representation of submarine landslides and generated surface waves.

The model is described by the following system of PDEs:

$$\begin{cases} (h_1)_t + (q_1\cos\theta)_x = 0, \\ (q_1)_t + \left(h_1u_1^2\cos\theta + \dfrac{g}{2}h_1^2\cos^3\theta\right)_x = -gh_1\cos\theta B_x - \dfrac{g}{2}h_1^2\cos^2\theta(\cos\theta)_x \\ \qquad\qquad - gh_1\cos\theta(h_2\cos^2\theta)_x + \phi_1, \\ (h_2)_t + (q_2\cos\theta)_x = 0, \\ (q_2)_t + \left(h_2u_2^2\cos\theta + \dfrac{g}{2}\Lambda_2h_2^2\cos^3\theta\right)_x = -gh_2\cos\theta B_x - \dfrac{g}{2}h_2^2\cos^2\theta(\cos\theta)_x \\ \qquad\qquad - r\Lambda_1gh_2\cos\theta(h_1\cos^2\theta)_x - \phi_2 + \dfrac{\mathcal{T}}{\cos\theta}, \end{cases} \tag{1.1}$$

where $h_1(x,t)$ and $h_2(x,t)$ are the depths of the upper and lower layers, respectively, $u_1(x,t)$ and $u_2(x,t)$ are the corresponding layer velocities, $q_1 = h_1u_1$ and $q_2 = h_2u_2$ are the discharges, $B(x)$ is the function that represents a non-erodible bottom, $\theta(x)$ is the angle of $B(x)$ from horizontal, g is the gravitational constant, $r = \rho_1/\rho_2$ is the constant ratio of the densities, Λ_1 and Λ_2 are physical parameters relating anisotropy or normal stress on each layer and the porosity of each layer, $\phi_i = \frac{\text{fric}(u_1,u_2)}{\cos\theta\rho_i}$ is the inter-layer friction, $\mathcal{T} = \mathcal{T}(h_2,u_2;\delta_0)$ is the Coulomb friction term that describes the friction between the lower layer and the bottom, and δ_0 is a physical parameter of the fluid-granular mixture known as the angle of repose. The physical setting is laid out in Figure 1.

The system (1.1) was derived from the incompressible Euler equations wherein the assumption is made that the lower layer is comprised of a mixture of granular and fluid particles that move at the same velocity, while the upper layer is solely fluid. As a result, the two

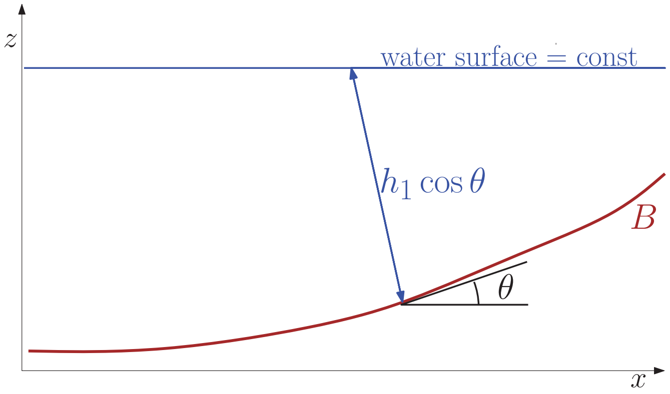

Figure 2. Diagram depicting the "lake-at-rest" steady-state. In the absence of a lower layer, the system reduces to a single-layer shallow water system.

layers have different constant densities $\rho_1 < \rho_2$ and are not necessarily immiscible. The resulting system is obtained by a vertical averaging across each layer depth. For details concerning the derivation of the system, see [14].

Our goal is to develop a highly accurate and robust numerical method for the system (1.1). Numerically studying the system (1.1) presents many of the same challenges seen in multilayer shallow water models (see, e.g., [1, 9–12, 25, 28]). It contains nonconservative product terms, it is only conditionally hyperbolic, and its eigenstructure cannot be obtained in explicit form. A good scheme for (1.1) should be well-balanced (it should exactly preserve steady-state solutions), it should preserve positivity of both h_1 and h_2, it should be able to properly handle discontinuous/nonsmooth solutions, and it should also be insensitive to the way the nonconservative terms are discretized. In this paper, we develop a new central-upwind scheme for (1.1) which possesses all of these features.

Central-upwind schemes (first introduced in [26] and further developed in [21, 22]) are Godunov-type finite volume methods. They belong to the class of Riemann-problem-solver-free central schemes and thus can be applied to a variety of hyperbolic systems of conservation laws as a "black-box" solver. When central-upwind schemes are applied to systems of balance laws, a special treatment of the source, friction, nonconservative product and more terms appearing in the system at hand must be developed. This was done for single- and two-layer shallow water models in [8, 20, 23–25]. To apply the central-upwind scheme to (1.1), one needs to specify the way the terms on the right-hand side are discretized. This should be done in such a way that (i) physically relevant steady-state solutions are exactly preserved; (ii) h_1 and h_2 are guaranteed to be nonnegative; both (iii) nonconservative and (iv) friction terms are properly discretized.

(i) The first property a good numerical method for the system (1.1) must satisfy is that it must be well-balanced. That is, it should preserve the "lake-at-rest" steady-state solution corresponding to the flat water surface in the absence of a lower-layer:

$$h_1 \cos^2\theta + B \equiv \text{const}, \quad h_2 \equiv 0, \quad q_1 \equiv q_2 \equiv 0,$$

see Figure 2. Preserving this particular steady-state would guarantee that no artificial surface waves are generated, and also ensure that small perturbations of either the surface or the lower layer will not lead to a "numerical storm".

(ii) Good numerical methods should also preserve positivity of h_1 and h_2 since solutions containing negative h_1 or h_2 would be nonphysical and will cause the numerical computations to fail. To ensure positivity of h_1 and h_2, we follow the idea from [23]. We first replace the bottom topography with its continuous piecewise linear approximation and then adjust the piecewise linear reconstruction of the water heights, assuring that through each computational cell the depth of each layer is nonnegative. This will lead to a method which is both well-balanced and positivity preserving.

(iii) Another challenge in the development of reliable and robust numerical methods is the discretization of the nonconservative products on the right-hand side of (1.1). In many cases, changing the way these terms are discretized may lead to qualitatively different computed solutions. An ultimate goal is to develop a method for which the computed solution would be insensitive to the way nonconservative terms are discretized. To address this problem, we follow the approach proposed in [25] by rewriting the system in an equivalent form that allows for "favorable" treatment of the nonconservative products. This approach uses the fact that in all practical oceanographic applications, *fluctuations* in the total water level, denoted by $\varepsilon := h_1\cos^2\theta + h_2\cos^2\theta + B$, are typically much smaller than the total water depth. To take advantage of this fact, the system is rewritten in a way so that the nonconservative product terms become proportional to ε, which will reduce the impact that the particular discretization of nonconservative terms has on the overall computed solution.

(iv) The final challenge with the system (1.1) is treatment of the Coulomb friction term $\mathcal{T}$. We use an operator splitting method in which the nonconservative products and geometric source terms are first applied to reach an intermediate solution, and then we apply a friction mechanism that slows or stops the lower layer in each computational cell depending on the value of the discharge there.

All of these goals (i)–(iv) are achieved. In Section 2, we rewrite the system (1.1) in a computationally favorable form. In Section 3, we derive the central-upwind scheme for the reformulated system. In particular: in Section 3.3, we introduce the measures that preserve positivity; in Section 3.4, we derive a well-balanced discretization of the geometric source terms; in Section 3.5, we write down a proper discretization of the nonconservative terms; in Section 3.6, we show how to address the Coulomb friction. Finally, in Section 4, the new scheme is successfully applied to various test problems.

2. Reformulated System

We define the variables $w_i := h_i\cos^2\theta$, $i = 1, 2$ and $\varepsilon := w_1 + w_2 + B$, for which the "lake-at-rest" steady state is given by

$$\varepsilon \equiv \text{const}, \quad w_2 \equiv 0, \quad q_1 \equiv q_2 \equiv 0. \tag{2.1}$$

In this paper, we will neglect the interlayer friction terms ϕ_1 and ϕ_2, and let $\Lambda_1 = \Lambda_2 = 1$, which corresponds to the two layers being immiscible. The system (1.1) can then be rewritten in terms of the equilibrium variables $\mathbf{U} := (\varepsilon, q_1, w_2, q_2)^T$ as follows:

$$\begin{cases} \varepsilon_t + ((q_1+q_2)\cos^3\theta)_x = 2(q_1+q_2)\cos^2\theta(\cos\theta)_x, \\ (q_1)_t + \Big(\dfrac{q_1^2\cos^3\theta}{\varepsilon-(w_2+B)} + \dfrac{g}{2}\dfrac{\varepsilon^2-2\varepsilon(w_2+B)}{\cos\theta}\Big)_x = -\dfrac{g}{\cos\theta}\varepsilon(w_2+B)_x \\ \qquad\qquad - \dfrac{g}{2}\dfrac{\varepsilon^2-2\varepsilon(w_2+B)}{\cos^2\theta}(\cos\theta)_x, \\ (w_2)_t + (q_2\cos^3\theta)_x = 2q_2\cos^2\theta(\cos\theta)_x, \\ (q_2)_t + \Big(\dfrac{q_2^2\cos^3\theta}{w_2} + \dfrac{g}{2}\dfrac{(1-r)w_2^2+2rw_2\varepsilon}{\cos\theta}\Big)_x = -\dfrac{(1-r)g}{\cos\theta}w_2B_x + \dfrac{rg}{\cos\theta}\varepsilon(w_2)_x \\ \qquad\qquad - \dfrac{g}{2}\dfrac{(1-r)w_2^2+2r\varepsilon w_2}{\cos^2\theta}(\cos\theta)_x + \dfrac{\mathcal{T}}{\cos\theta}. \end{cases} \tag{2.2}$$

For smooth solutions, this system is equivalent to the original system (1.1). We also shift the z-coordinate so that the water surface reference level is 0 (see Figure 3). This means that for the "lake-at-rest" steady state (2.1), $\varepsilon \equiv 0$, and in all practical applications ε will remain small relative to the total depth of the water (w_1+w_2). The system (2.2) is favorable for numerical computations because the nonconservative product $\varepsilon(w_2)_x$ appearing on the right-hand side of (2.2) is proportional to ε.

3. Numerical Scheme

We develop a new well-balanced positivity preserving scheme for (2.2). Our scheme is based on the semi-discrete central-upwind scheme from [22] (see also [23, 25]). For simplicity, we introduce a uniform grid $x_\alpha = \alpha\Delta x$ where Δx is a small spatial scale, and denote the computational cells by $I_j := [x_{j-\frac12}, x_{j+\frac12}]$.

3.1. Linear Bottom

We replace the bottom topography function $B(x)$ with its continuous piecewise linear approximation $\widetilde{B}(x)$ that connects the points $(x_{j-\frac12}, B(x_{j-\frac12}))$ and $(x_{j+\frac12}, B(x_{j+\frac12}))$:

$$\widetilde{B}(x) = B_{j-\frac12} + (B_{j+\frac12} - B_{j-\frac12})\frac{x - x_{j-\frac12}}{\Delta x}, \quad x_{j-\frac12} < x < x_{j+\frac12},$$

where $B_{j+\frac12} := B(x_{j+\frac12})$. Replacing B with $\widetilde{B}$ does not affect the formal accuracy of the scheme since the piecewise linear interpolant is a second-order approximation of B. The piecewise linear function $\widetilde{B}$ has the following property:

$$B_j := \widetilde{B}(x_j) = \frac{1}{\Delta x}\int_{I_j} \widetilde{B}(x)\,dx = \frac{B_{j+\frac12} + B_{j-\frac12}}{2}.$$

This is important for the positivity preserving property of the scheme. This procedure is exactly the same as in [23, 25].

In our scheme, we will need to have the values of $\cos\theta$ and $\sin\theta$ at the cell interfaces $x = x_{j+\frac12}$. These values will be calculated using the original function B, that is, we take

$$\cos\theta_{j+\frac12} := \cos(\theta(x_{j+\frac12})) = \cos(\arctan(B'(x_{j+\frac12}))),$$
$$\sin\theta_{j+\frac12} := \sin(\theta(x_{j+\frac12})) = \sin(\arctan(B'(x_{j+\frac12}))).$$

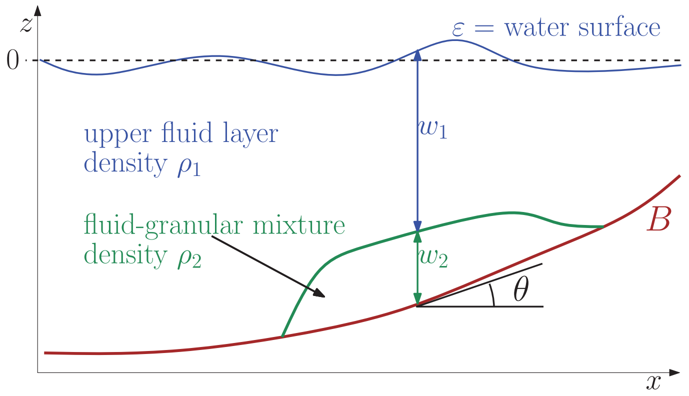

Figure 3. Diagram depicting the variables in the new system. The z-coordinate is shifted so that the bottom B is negative and the water surface reference level is 0. In practical applications, this ensures that the water surface ε is small since it is close to the reference level (dashed line).

3.2. The Semi-Discrete Central-Upwind Scheme

First, we introduce notations for the flux $\mathbf{F}$, the geometric source term $\mathbf{S}$, the nonconservative products $\mathbf{N}$, and the Coulomb friction $\mathbf{C}$:

$$\begin{aligned}
\mathbf{F}(\mathbf{U},B) &:= \begin{pmatrix} (q_1+q_2)\cos^3\theta \\ \frac{q_1^2\cos^3\theta}{\varepsilon-(w_2+B)} + \frac{g}{2}\frac{\varepsilon^2-2\varepsilon(w_2+B)}{\cos\theta} \\ q_2\cos^3\theta \\ \frac{q_2^2\cos^3\theta}{w_2} + \frac{g}{2}\frac{(1-r)w_2^2+2rw_2\varepsilon}{\cos\theta} \end{pmatrix}, \\
\mathbf{S}(\mathbf{U},B) &:= \begin{pmatrix} 2(q_1+q_2)\cos^2\theta(\cos\theta)_x \\ -\frac{g}{\cos\theta}\,\varepsilon B_x - \frac{g}{2}\frac{\varepsilon^2-2\varepsilon(w_2+B)}{\cos^2\theta}(\cos\theta)_x \\ 2q_2\cos^2\theta(\cos\theta)_x \\ -\frac{(1-r)g}{\cos\theta}w_2B_x - \frac{g}{2}\frac{(1-r)w_2^2+2r\varepsilon w_2}{\cos^2\theta}(\cos\theta)_x \end{pmatrix}, \\
\mathbf{N}(\mathbf{U},B) &:= \left(0, -\frac{g\varepsilon}{\cos\theta}(w_2)_x, 0, \frac{rg\varepsilon}{\cos\theta}(w_2)_x\right)^T, \\
\mathbf{C}(\mathbf{U},B) &:= \left(0,0,0,\frac{\mathcal{T}}{\cos\theta}\right)^T,
\end{aligned} \tag{3.1}$$

so that the system (2.2) can be written as

$$\mathbf{U}_t + \mathbf{F}(\mathbf{U},B)_x = \mathbf{S}(\mathbf{U},B) + \mathbf{N}(\mathbf{U},B) + \mathbf{C}(\mathbf{U},B). \tag{3.2}$$

Using these notations, a semi-discrete finite-volume scheme for (3.2) takes the form of the following system of time-dependent ODEs:

$$\frac{d}{dt}\overline{\mathbf{U}}_j(t) = -\frac{\mathbf{H}_{j+\frac{1}{2}}(t) - \mathbf{H}_{j-\frac{1}{2}}(t)}{\Delta x} + \overline{\mathbf{S}}_j(t) + \overline{\mathbf{N}}_j(t) + \overline{\mathbf{C}}_j(t), \tag{3.3}$$

where $\overline{\mathbf{U}}_j(t)$ are approximations of the cell averages of the solution over the corresponding cells,

$$\overline{\mathbf{U}}_j(t) \approx \frac{1}{\Delta x}\int_{I_j}\mathbf{U}(x,t)\,dx,$$

$\mathbf{H}_{j+\frac{1}{2}}(t)$ are numerical fluxes, and $\overline{\mathbf{S}}_j(t)$ and $\overline{\mathbf{N}}_j(t)$ are discretizations of the cell averages of the geometric source and nonconservative product terms, respectively:

$$\overline{\mathbf{S}}_j(t) \approx \frac{1}{\Delta x}\int_{I_j} \mathbf{S}(\mathbf{U}(x,t),B(x))\,dx, \quad \overline{\mathbf{N}}_j(t) \approx \frac{1}{\Delta x}\int_{I_j} \mathbf{N}(\mathbf{U}(x,t),B(x))\,dx.$$

The contribution of $\mathbf{C}$ will be discussed in Section 3.6 below.

The central-upwind numerical fluxes $\mathbf{H}_{j+\frac{1}{2}}$ are the ones proposed in [22] (see also [23,25]):

$$\mathbf{H}_{j+\frac{1}{2}}(t) = \frac{a^+_{j+\frac{1}{2}}\mathbf{F}(\mathbf{U}^-_{j+\frac{1}{2}},B_{j+\frac{1}{2}}) - a^-_{j+\frac{1}{2}}\mathbf{F}(\mathbf{U}^+_{j+\frac{1}{2}},B_{j+\frac{1}{2}})}{a^+_{j+\frac{1}{2}} - a^-_{j+\frac{1}{2}}} + \frac{a^+_{j+\frac{1}{2}}a^-_{j+\frac{1}{2}}}{a^+_{j+\frac{1}{2}} - a^-_{j+\frac{1}{2}}}\big[\mathbf{U}^+_{j+\frac{1}{2}} - \mathbf{U}^-_{j+\frac{1}{2}}\big]. \tag{3.4}$$

Here, the values $\mathbf{U}^\pm_{j+\frac{1}{2}}$ are the right/left point values at $x = x_{j+\frac{1}{2}}$ of the conservative piecewise linear reconstruction $\widetilde{\mathbf{U}}$,

$$\widetilde{\mathbf{U}}(x) := \overline{\mathbf{U}}_j + (\mathbf{U}_x)_j(x - x_j), \quad x_{j-\frac{1}{2}} < x < x_{j+\frac{1}{2}}, \tag{3.5}$$

which is used to approximate $\mathbf{U}$ at time t, that is,

$$\mathbf{U}^\pm_{j+\frac{1}{2}} := \widetilde{\mathbf{U}}(x_{j+\frac{1}{2}} \pm 0) = \overline{\mathbf{U}}_{j+\frac{1}{2}\pm\frac{1}{2}} \mp \frac{\Delta x}{2}(\mathbf{U}_x)_{j+\frac{1}{2}\pm\frac{1}{2}}. \tag{3.6}$$

The numerical derivatives $(\mathbf{U}_x)_j$ are at least first-order accurate componentwise approximations of $\mathbf{U}_x(x_j,t)$, computed using a nonlinear limiter needed to ensure the non-oscillatory nature of the reconstruction (3.5). The right- and left-sided local speeds $a^\pm_{j+\frac{1}{2}}$ in (3.4) are obtained from the smallest and largest eigenvalues of the Jacobian $\frac{\partial \mathbf{F}}{\partial \mathbf{U}}$ (see Section 3.7 for details). Notice that the terms $\mathbf{U}^\pm_{j+\frac{1}{2}}$, $\overline{\mathbf{U}}_j$, $a^\pm_{j+\frac{1}{2}}$, $\widetilde{\mathbf{U}}(x)$ and $(\mathbf{U}_x)_j$ all depend on t, but we suppress this dependence for simplicity.

A fully discrete central-upwind scheme is obtained by applying an appropriate ODE solver to (3.3). In our computations, we have used the third-order strong stability preserving Runge–Kutta (SSP-RK) method from [15], which ensures a non-oscillatory nature of the resulting fully discrete scheme.

3.3. Positivity Preserving Reconstruction

The evaluation of the numerical derivatives $(\mathbf{U}_x)$ in equation (3.5) is essential to the non-oscillatory property and nonlinear stability of the scheme. One can achieve these attributes by using a nonlinear limiter, which ensures the reconstruction is non-oscillatory. The central-upwind scheme can be implemented with any one of the many nonlinear limiters available. In the numerical experiments presented in Section 4, we have used the generalized minmod limiter:

$$(\mathbf{U}_x)_j = \mathrm{minmod}\Big(\gamma\frac{\overline{\mathbf{U}}_j - \overline{\mathbf{U}}_{j-1}}{\Delta x}, \frac{\overline{\mathbf{U}}_{j+1} - \overline{\mathbf{U}}_{j-1}}{2\Delta x}, \gamma\frac{\overline{\mathbf{U}}_{j+1} - \overline{\mathbf{U}}_j}{\Delta x}\Big), \quad \gamma \in [1,2], \tag{3.7}$$

where the minmod function is defined as

$$\mathrm{minmod}(z_1,z_2,\dots) := \begin{cases} \min_j\{z_j\}, & \text{if } z_j > 0 \text{ for all } j,\\ \max_j\{z_j\}, & \text{if } z_j < 0 \text{ for all } j,\\ 0, & \text{otherwise,} \end{cases}$$

and the parameter γ can be used to control the amount of numerical viscosity present in the resulting scheme (see, e.g., [27,31,33] for more details concerning nonlinear limiters).

The use of nonlinear limiters, however, is not enough to guarantee positivity of the reconstructed point values $(w_2)^{\pm}_{j+\frac{1}{2}}$ and $(w_1)^{\pm}_{j+\frac{1}{2}}$ even when the cell averages

$$(\overline{w}_2)_j = \overline{\mathbf{U}}^{(3)}_j \quad \text{and} \quad (\overline{w}_1)_j = \overline{\mathbf{U}}^{(1)}_j - \overline{\mathbf{U}}^{(3)}_j - B_j = \overline{\varepsilon}_j - (\overline{w}_2)_j - B_j$$

are positive for all j. We follow the procedure presented in [25] and [23] by amending our reconstruction with the following two positivity correction steps:

$$\begin{aligned}
&\text{if } (w_2)^{-}_{j+\frac{1}{2}} < 0, \text{ then take } ((w_2)_x)_j := -\frac{(\overline{w}_2)_j}{\Delta x/2} \\
&\qquad\Longrightarrow (w_2)^{-}_{j+\frac{1}{2}} = 0, \quad (w_2)^{+}_{j-\frac{1}{2}} = 2(\overline{w}_2)_j, \\
&\text{if } (w_2)^{+}_{j-\frac{1}{2}} < 0, \text{ then take } ((w_2)_x)_j := \frac{(\overline{w}_2)_j}{\Delta x/2} \\
&\qquad\Longrightarrow (w_2)^{-}_{j+\frac{1}{2}} = 2(\overline{w}_2)_j, \quad (w_2)^{+}_{j-\frac{1}{2}} = 0,
\end{aligned} \tag{3.8}$$

and

$$\begin{aligned}
&\text{if } \varepsilon^{-}_{j+\frac{1}{2}} < (w_2)_{j+\frac{1}{2}} + B_{j+\frac{1}{2}}, \text{ then take } (\varepsilon_x)_j := \frac{(w_2)_{j+\frac{1}{2}} + B_{j+\frac{1}{2}} - \overline{\varepsilon}_j}{\Delta x/2} \\
&\qquad\Longrightarrow \varepsilon^{-}_{j+\frac{1}{2}} = (w_2)_{j+\frac{1}{2}} + B_{j+\frac{1}{2}}, \quad \varepsilon^{+}_{j-\frac{1}{2}} = 2\overline{\varepsilon}_j - (w_2)_{j+\frac{1}{2}} - B_{j+\frac{1}{2}}, \\
&\text{if } \varepsilon^{+}_{j-\frac{1}{2}} < (w_2)_{j-\frac{1}{2}} + B_{j-\frac{1}{2}}, \text{ then take } (\varepsilon_x)_j := \frac{\overline{\varepsilon}_j - (w_2)_{j-\frac{1}{2}} + B_{j-\frac{1}{2}}}{\Delta x/2} \\
&\qquad\Longrightarrow \varepsilon^{-}_{j+\frac{1}{2}} = 2\overline{\varepsilon}_j - (w_2)_{j-\frac{1}{2}} - B_{j-\frac{1}{2}}, \quad \varepsilon^{+}_{j-\frac{1}{2}} = (w_2)_{j-\frac{1}{2}} + B_{j-\frac{1}{2}}.
\end{aligned} \tag{3.9}$$

Following these steps will ensure that the reconstructed point values of w_1 and w_2 will be nonnegative so long as the cell averages are nonnegative.

Another critical point to the positivity preserving nature of our scheme is the computation of the velocity variables $u_i = q_i \cos^2\theta / w_i$, which are needed for calculating the numerical fluxes (Section 3.2) as well as for estimating the wave speeds (Section 3.7). Even though we have guaranteed that the quantities $(w_i)^{\pm}_{j+\frac{1}{2}}$ will be nonnegative, they may be small or even zero. Therefore, a desingularization procedure is required in this computation. We again follow [25] and [23] and compute the velocities using the following formula:

$$u_i := \frac{\sqrt{2}\, w_i \cdot q_i \cos^2\theta}{\sqrt{w_i^4 + \max\left(w_i^4, \beta\right)}}, \quad i = 1, 2, \tag{3.10}$$

where β is a small desingularization parameter (in our experiments $\beta = \min\{(\Delta x)^3, 10^{-4}\}$). This reduces to $u_i = q_i \cos^2\theta / w_i$ for large values of w_i and the velocities u_i will be modified according to (3.10) only at those cell interfaces where the reconstructed values of w_i are small. Notice that after this, the discharges at the same points have to be modified by setting

$$q_i = \frac{w_i \cdot u_i}{\cos^2\theta}, \quad i = 1, 2 \tag{3.11}$$

there. This will be crucial to have a positivity preserving scheme as it is proved in Theorem 3.1 (see Section 3.8).

3.4. Well-Balanced Discretization

An essential aspect to a good numerical scheme for the system (2.2) is that it does not result in the so-called "numerical storm", that is, any surface waves should be purely physical and not artifacts of the numerical scheme. Therefore we design our scheme to be well-balanced, and that will ensure that small perturbations of steady states will not grow in a manner that is not physical.

In many previous well-balanced schemes for two-layer shallow water models (see, e.g., [1, 5, 10–12, 25]), the preserved steady state corresponded to the case of both layers being flat and motionless (for the system (2.2) this would be $\varepsilon = \text{const}$ with $w_2 + B = \text{const}$). Because of the friction and ratio of densities r that we would see in practical applications of this model, we do not expect that this steady-state will ever be achieved. When the lower layer slides down the bottom and stops due to friction, it will not be flat, but will be in some mound shape. At this point, the lower layer will essentially become a part of the bottom topography while the upper layer will continue to flow as in the case of a single-layer shallow water system. Therefore, we choose to preserve another "lake-at-rest" steady state that corresponds to the absence of the lower layer, in which case the model acts like a single-layer shallow water model.

Our goal is to design a numerical scheme that exactly preserves this "lake-at-rest" steady-state solution ($\varepsilon = \text{const}$, $w_2 = 0$, $q_1 = q_2 = 0$). For brevity we denote $\cos\theta_{j+\frac12}$ by $c_{j+\frac12}$ and substitute the steady-state data $\overline{\varepsilon}_j = \varepsilon$, $(\overline{w}_2)_j = (\overline{q}_1)_j = (\overline{q}_2)_j = 0$ for all j into the second component of the numerical flux (3.4). We obtain

$$\mathbf{H}^{(2)}_{j+\frac12} = \frac{g}{2}\,\frac{\varepsilon(\varepsilon - 2B_{j+\frac12})}{c_{j+\frac12}},$$

and thus

$$\begin{aligned}
-\frac{\mathbf{H}^{(2)}_{j+\frac12} - \mathbf{H}^{(2)}_{j-\frac12}}{\Delta x} &= -\frac{g}{2}\,\frac{\varepsilon(\varepsilon - 2B_{j+\frac12})}{\Delta x c_{j+\frac12}} + \frac{g}{2}\,\frac{\varepsilon(\varepsilon - 2B_{j-\frac12})}{\Delta x c_{j-\frac12}}\\
&= \frac{g\varepsilon}{2\Delta x c_{j+\frac12}c_{j-\frac12}}\Big[c_{j-\frac12}(2B_{j+\frac12} - \varepsilon) - c_{j+\frac12}(2B_{j-\frac12} - \varepsilon)\Big]\\
&= \frac{g\varepsilon}{2\Delta x c_{j+\frac12}c_{j-\frac12}}\bigg[\varepsilon(c_{j+\frac12} - c_{j-\frac12}) + 2\bigg(\frac{c_{j+\frac12} + c_{j-\frac12}}{2}(B_{j+\frac12} - B_{j-\frac12})\\
&\qquad - \frac{B_{j+\frac12} + B_{j-\frac12}}{2}(c_{j+\frac12} - c_{j-\frac12})\bigg)\bigg]\\
&= g\varepsilon\,\frac{c_{j+\frac12} + c_{j-\frac12}}{2c_{j+\frac12}c_{j-\frac12}}\cdot\frac{B_{j+\frac12} - B_{j-\frac12}}{\Delta x}\\
&\qquad + \frac{g\varepsilon}{2c_{j+\frac12}c_{j-\frac12}}\big[\varepsilon - (B_{j+\frac12} + B_{j-\frac12})\big]\frac{c_{j+\frac12} - c_{j-\frac12}}{\Delta x},
\end{aligned} \tag{3.12}$$

which is the second component of the flux difference on the right-hand side of (3.3) at the "lake-at-rest" steady state. Since at this steady state, both $\mathbf{N}$ and $\mathbf{C}$ are zero, the scheme will be well-balanced provided the quadrature for the geometric source $\overline{\mathbf{S}}^{(2)}_j$ cancels the flux contribution (3.12). Such a quadrature can be easily constructed and it is

$$
\begin{aligned}
\overline{\mathbf{S}}_j^{(2)} &= -g\overline{\varepsilon}_j\,\frac{c_{j+\frac12}+c_{j-\frac12}}{2c_{j+\frac12}c_{j-\frac12}}\cdot\frac{B_{j+\frac12}-B_{j-\frac12}}{\Delta x}\\
&\qquad-\frac{g\overline{\varepsilon}_j}{2c_{j+\frac12}c_{j-\frac12}}\left[\overline{\varepsilon}_j-2(\overline{w}_2)_j-(B_{j+\frac12}+B_{j-\frac12})\right]\frac{c_{j+\frac12}-c_{j-\frac12}}{\Delta x}.
\end{aligned}
\tag{3.13}
$$

Since the first, third, and fourth components of $\mathbf{S}$ vanish at the "lake-at-rest" steady state, any consistent discretization of $\mathbf{S}^{(1)}$, $\mathbf{S}^{(3)}$, $\mathbf{S}^{(4)}$ can be used without affecting the well-balanced property of the scheme. In our numerical experiments we have used the following discretizations:

$$
\begin{aligned}
\overline{\mathbf{S}}_j^{(1)} &= 2((\overline{q}_1)_j+(\overline{q}_2)_j)c_{j+\frac12}c_{j-\frac12}\,\frac{c_{j+\frac12}-c_{j-\frac12}}{\Delta x},\\
\overline{\mathbf{S}}_j^{(3)} &= 2(\overline{q}_2)_jc_{j+\frac12}c_{j-\frac12}\,\frac{c_{j+\frac12}-c_{j-\frac12}}{\Delta x},\\
\overline{\mathbf{S}}_j^{(4)} &= -(1-r)g\,\frac{c_{j+\frac12}+c_{j-\frac12}}{2c_{j+\frac12}c_{j-\frac12}}(\overline{w}_2)_j\,\frac{B_{j+\frac12}-B_{j-\frac12}}{\Delta x}\\
&\qquad-g\,\frac{[(1-r)(\overline{w}_2)_j+2r\overline{\varepsilon}_j](\overline{w}_2)_j}{2c_{j+\frac12}c_{j-\frac12}}\cdot\frac{c_{j+\frac12}-c_{j-\frac12}}{\Delta x}.
\end{aligned}
\tag{3.14}
$$

Recall that in (3.13) and (3.14), we have used the notation $c_{j+\frac12}:=\cos\theta_{j+\frac12}$.

3.5. Nonconservative Terms

As mentioned in Section 1, an integral part of designing a stable numerical method for (1.1) is a proper treatment of the nonconservative products. However, now that we have rewritten the system (1.1) in a favorable way (2.2), the particular discretization of these terms will have only a small impact on the computed solution. This is because the surface waves in this model are typically several orders of magnitude smaller than the inertial waves, and thus after shifting our coordinate system the water surface ε is at or near zero in all practically relevant applications.

In this paper, we discretize the nonconservative product term $\overline{\mathbf{N}}_j$ as follows:

$$
\overline{\mathbf{N}}_j^{(2)} = -g\Big(\frac{\cos\theta_{j+\frac12}+\cos\theta_{j-\frac12}}{2\cos\theta_{j+\frac12}\cos\theta_{j-\frac12}}\Big)\cdot\overline{\varepsilon}_j((w_2)_x)_j,\quad \overline{\mathbf{N}}_j^{(4)}=-r\overline{\mathbf{N}}_j^{(2)}.
\tag{3.15}
$$

3.6. Coulomb Friction

To include the friction term into the model, we apply an operator splitting to the semi-discrete system (3.3). We split it into

$$
\begin{cases}
\dfrac{d}{dt}\overline{\mathbf{U}}_j = -\dfrac{\mathbf{H}_{j+\frac12}-\mathbf{H}_{j-\frac12}}{\Delta x}+\overline{\mathbf{S}}_j+\overline{\mathbf{N}}_j,\\[2mm]
\dfrac{d}{dt}\overline{\mathbf{U}}_j = \overline{\mathbf{C}}_j.
\end{cases}
\tag{3.16}
$$

This entails composing the two solution operators corresponding to each equation in (3.16) in the following manner:

$$
\mathbf{U}(t+\Delta t)\approx\mathcal{S}_{\mathbf{C}}(\Delta t)\mathcal{S}_{\mathbf{FSN}}(\Delta t)\mathbf{U}(t),
\tag{3.17}
$$

where $\mathcal{S}_{\mathbf{FSN}}$ and $\mathcal{S}_{\mathbf{C}}$ denote the corresponding solution operators. We first obtain $\mathbf{U}^* = \mathcal{S}_{\mathbf{FSN}}(\Delta t)\mathbf{U}(t)$ by applying the third-order SSP-RK solver from [15] to the scheme described above. We then apply the friction term by computing the same quantities as in [14], but rather than including them in the flux term, we treat the friction as a source term in our numerical method. This is a very straightforward approach because we do not have to adjust our numerical fluxes, and thus it is very simple to implement. This is achieved by updating the fourth component according to the following steps:

$$(\overline{q}_2)_j(t+\Delta t) = \begin{cases} (\overline{q}_2^*)_j + \mathcal{T}_j\Delta t, & \text{if } |(\overline{q}_2^*)_j| > \sigma_j^*\Delta t/\cos\theta_j, \\ 0, & \text{otherwise}, \end{cases} \tag{3.18}$$

with

$$\mathcal{T}_j := -\operatorname{sgn}\{(\overline{q}_2^*)_j\}\Big[\sigma_j^* + \frac{(\widehat{w}_2)_{j+\frac12} + (\widehat{w}_2)_{j-\frac12}}{2}\cdot(\widehat{u}_2)_j^2\cdot\frac{\sin\theta_{j+\frac12} - \sin\theta_{j-\frac12}}{\Delta x}\cdot\tan\delta_0\Big], \tag{3.19}$$

where

$$\begin{aligned} \sigma_j^* &:= g(1-r)\,\frac{(\widehat{w}_2)_{j+\frac12} + (\widehat{w}_2)_{j-\frac12}}{2}(\cos\theta_j)^2\tan\delta_0, \\ (\widehat{u}_2)_j &:= \frac{\sqrt{2}(\overline{w}_2^*)_j(\overline{q}_2^*)_j(\cos\theta_j)^2}{\sqrt{((\overline{w}_2^*)_j)^4 + \max\left(((\overline{w}_2^*)_j)^4, \beta\right)}}, \\ (\widehat{w}_2)_{j+\frac12} &:= \frac12\Big(\frac{(\overline{w}_2^*)_j}{(\cos\theta_j)^2} + \frac{(\overline{w}_2^*)_{j+1}}{(\cos\theta_{j+1})^2}\Big), \end{aligned} \tag{3.20}$$

and β is the same small desingularization parameter as in equation (3.10). These are exactly the same quantities as were calculated in [14] with the exception of $(\widehat{u}_2)_j$, which we modify by including the desingularization procedure.

The operator $\mathcal{S}_{\mathbf{C}}$ determines in each cell I_j whether the momentum of the lower layer is below some critical threshold which depends on the slope of the bottom B_x and the angle of repose of the granular layer δ_0, a given physical parameter. If so, then the mass is stopped in that cell (the momentum q_2 is set to zero there), and if not, the mass is slowed down by adding $\mathcal{T}_j\Delta t$, which has the opposite sign to the momentum $(\overline{q}_2^*)_j$. For more information on the Coulomb friction associated with this system, we refer the reader to [29].

Remark 3.1. Desingularization is critical to the success of the friction procedure since the locations where (w_2) is small are exactly where one would expect the friction cause the lower layer to stop. Without desingularization, the velocities $(\widehat{u}_2)$ at these locations may become very large, and as a result the momentum may never fall below the critical threshold $\sigma^*\Delta t/\cos\theta$.

3.7. Calculating Wave Speeds

To calculate wave speeds, we need bounds on the eigenvalues of the Jacobian of the flux term in the system (2.2). To achieve this, we write the characteristic equation in the form

$$\lambda^4 + c_1\lambda^3 + c_2\lambda^2 + c_3\lambda + c_4 = 0 \tag{3.21}$$

with coefficients

$$\begin{aligned}
c_1 &= -2\cos\theta(u_1+u_2),\\
c_2 &= \cos^2\theta\big((u_1+u_2)^2+2u_1u_2+gB-(1+r)g\varepsilon\big),\\
c_3 &= 2\cos^3\theta\big(u_1u_2(u_1+u_2)-gu_2w_1-gu_1(r\varepsilon+w_2)\big),\\
c_4 &= \cos^4\theta\big[u_1^2u_2^2-g\big(u_1^2(r\varepsilon+w_2)+u_2^2(B+\varepsilon-w_2)\big)\\
&\qquad +g^2\big((B+\varepsilon)(r\varepsilon+(1-r)w_2)-(1-r)w_2^2\big)\big].
\end{aligned}$$

We then use the Lagrange theorem (see, e.g., [30]) to establish bounds on the roots of the polynomial (3.21) as was done in [25]. This theorem says that the largest nonnegative root of (3.21) is smaller than the sum of the largest and second largest numbers in the set $\{\sqrt[j]{|c_j|}\,:\,j\in J_{\max}\}$, where $\{c_j\,:\,j\in J_{\max}\}$ is the set of negative coefficients of (3.21). Similarly, the smallest nonpositive root of (3.21) is larger than the sum of the smallest and second smallest numbers in the set $\{-\sqrt[j]{|d_j|}\,:\,j\in J_{\max}\}$ where $\{d_j\,:\,j\in J_{\max}\}$ is the set of negative coefficients of the polynomial

$$\lambda^4+d_1\lambda^3+d_2\lambda^2+d_3\lambda+d_4=0,\quad d_j=(-1)^jc_j\quad\text{for all } j.$$

Let us denote the bounds by

$$\begin{aligned}
(\lambda_{\max})^{\pm}_{j+\frac12} &:= \lambda_{\max}\big(\varepsilon^{\pm}_{j+\frac12},(w_2)^{\pm}_{j+\frac12},(u_1)^{\pm}_{j+\frac12},(u_2)^{\pm}_{j+\frac12}\big),\\
(\lambda_{\min})^{\pm}_{j+\frac12} &:= \lambda_{\min}\big(\varepsilon^{\pm}_{j+\frac12},(w_2)^{\pm}_{j+\frac12},(u_1)^{\pm}_{j+\frac12},(u_2)^{\pm}_{j+\frac12}\big).
\end{aligned}$$

Then the one-sided local propagation speeds needed to calculate the numerical flux (3.4), can be estimated by

$$\begin{aligned}
a^+_{j+\frac12} &= \max_{\pm}\big\{(\lambda_{\max})^{\pm}_{j+\frac12},\cos\theta_{j+\frac12}(u_1)^{\pm}_{j+\frac12},\cos\theta_{j+\frac12}(u_2)^{\pm}_{j+\frac12},0\big\},\\
a^-_{j+\frac12} &= \min_{\pm}\big\{(\lambda_{\min})^{\pm}_{j+\frac12},\cos\theta_{j+\frac12}(u_1)^{\pm}_{j+\frac12},\cos\theta_{j+\frac12}(u_2)^{\pm}_{j+\frac12},0\big\}.
\end{aligned}\tag{3.22}$$

Note that we also impose that the physical speeds of the layers $\cos\theta_{j+\frac12}(u_{1,2})^{\pm}_{j+\frac12}$ cannot exceed the local propagation speeds $a^{\pm}_{j+\frac12}$, which is critical for the positivity proof that follows in Section 3.8.

3.8. Proof of Positivity

Theorem 3.1. *Suppose the system* (2.2) *is numerically solved by the central-upwind semi-discrete scheme given by* (3.16) *and* (3.4) *with* (3.14), (3.15), (3.6)–(3.11), *and* (3.22). *Assume that the system of ODEs* (3.16) *is numerically integrated by the forward Euler method and that for all* j, $(\overline{w}_1)^n_j:=\overline{\varepsilon}^n_j-(\overline{w}_2)^n_j-B_j\geqslant 0$ *and* $(\overline{w}_2)^n_j\geqslant 0$.

Then, the depth of each layer remains nonnegative in time; that is, $(\overline{w}_1)^{n+1}_j:=\overline{\varepsilon}^{n+1}_j-(\overline{w}_2)^{n+1}_j-B_j\geqslant 0$ *and* $(\overline{w}_2)^{n+1}_j\geqslant 0$ *for all* j, *provided that* $\Delta t\leqslant\Delta x/(2a(1+\delta))$, *where* $a:=\max_j\{\max\{a^+_{j+\frac12},-a^-_{j+\frac12}\}\}$, $\delta:=\max_j\{\max\{\delta^+_j,\delta^-_j\}\}$, *and* $\delta^{\pm}_j$ *are*

$$\delta^+_j:=\frac{\cos\theta_{j+\frac12}}{\cos\theta_{j-\frac12}}\Big(\frac{\cos\theta_{j+\frac12}}{\cos\theta_{j-\frac12}}-1\Big),\quad \delta^-_j:=\frac{\cos\theta_{j-\frac12}}{\cos\theta_{j+\frac12}}\Big(1-\frac{\cos\theta_{j-\frac12}}{\cos\theta_{j+\frac12}}\Big).\tag{3.23}$$

Proof. Applying the forward Euler method to the first and third components of the ODE system (3.16) results in the following:

$$\overline{\varepsilon}_j^{n+1} = \overline{\varepsilon}_j^{n} - \lambda\big(\mathbf{H}^{(1)}_{j+\frac{1}{2}} - \mathbf{H}^{(1)}_{j-\frac{1}{2}}\big) + \Delta t \overline{\mathbf{S}}_j^{(1)}, \tag{3.24}$$

$$(\overline{w}_2)_j^{n+1} = (\overline{w}_2)_j^{n} - \lambda\big(\mathbf{H}^{(3)}_{j+\frac{1}{2}} - \mathbf{H}^{(3)}_{j-\frac{1}{2}}\big) + \Delta t \overline{\mathbf{S}}_j^{(3)}, \tag{3.25}$$

where $\lambda := \Delta t/\Delta x$ and the numerical fluxes are evaluated at time $t = t^n$.

We first show that if the cell averages $(\overline{w}_2)_j^n$ are nonnegative, then the new cell averages $(\overline{w}_2)_j^{n+1}$ are also nonnegative. Since, according to (3.1) and (3.4), the third component $\mathbf{H}^{(3)}_{j+\frac{1}{2}}$ of the central-upwind numerical flux is given by

$$\mathbf{H}^{(3)}_{j+\frac{1}{2}} = \frac{a^+_{j+\frac{1}{2}}(q_2)^-_{j+\frac{1}{2}}(\cos\theta_{j+\frac{1}{2}})^3 - a^-_{j+\frac{1}{2}}(q_2)^+_{j+\frac{1}{2}}(\cos\theta_{j+\frac{1}{2}})^3}{a^+_{j+\frac{1}{2}} - a^-_{j+\frac{1}{2}}} + \frac{a^+_{j+\frac{1}{2}}a^-_{j+\frac{1}{2}}}{a^+_{j+\frac{1}{2}} - a^-_{j+\frac{1}{2}}}\big[(w_2)^+_{j+\frac{1}{2}} - (w_2)^-_{j+\frac{1}{2}}\big], \tag{3.26}$$

and according to (3.14) the source is given by

$$\overline{\mathbf{S}}_j^{(3)} = 2(\overline{q}_2)_j \cos\theta_{j+\frac{1}{2}} \cos\theta_{j-\frac{1}{2}} \frac{\cos\theta_{j+\frac{1}{2}} - \cos\theta_{j-\frac{1}{2}}}{\Delta x}, \tag{3.27}$$

we use (3.11), (3.23), (3.26), and (3.27) to rewrite (3.25) as

$$\begin{aligned}
(\overline{w}_2)_j^{n+1} = {} & \Big[\frac{1}{2} + \lambda\Big\{a^-_{j-\frac{1}{2}}\Big(\frac{a^+_{j-\frac{1}{2}} - \cos\theta_{j-\frac{1}{2}}(u_2)^+_{j-\frac{1}{2}}}{a^+_{j-\frac{1}{2}} - a^-_{j-\frac{1}{2}}}\Big) + \cos\theta_{j-\frac{1}{2}}(u_2)^+_{j-\frac{1}{2}}\delta_j^+\Big\}\Big](w_2)^+_{j-\frac{1}{2}} \\
& + \Big[\frac{1}{2} - \lambda\Big\{a^+_{j+\frac{1}{2}}\Big(\frac{\cos\theta_{j+\frac{1}{2}}(u_2)^-_{j+\frac{1}{2}} - a^-_{j+\frac{1}{2}}}{a^+_{j+\frac{1}{2}} - a^-_{j+\frac{1}{2}}}\Big) - \cos\theta_{j+\frac{1}{2}}(u_2)^-_{j+\frac{1}{2}}\delta_j^-\Big\}\Big](w_2)^-_{j+\frac{1}{2}} \\
& - \lambda a^-_{j+\frac{1}{2}}\Big(\frac{a^+_{j+\frac{1}{2}} - \cos\theta_{j+\frac{1}{2}}(u_2)^+_{j+\frac{1}{2}}}{a^+_{j+\frac{1}{2}} - a^-_{j+\frac{1}{2}}}\Big)(w_2)^+_{j+\frac{1}{2}} \\
& + \lambda a^+_{j-\frac{1}{2}}\Big(\frac{\cos\theta_{j-\frac{1}{2}}(u_2)^-_{j-\frac{1}{2}} - a^-_{j-\frac{1}{2}}}{a^+_{j-\frac{1}{2}} - a^-_{j-\frac{1}{2}}}\Big)(w_2)^-_{j-\frac{1}{2}},
\end{aligned} \tag{3.28}$$

where we have used the facts that

$$(\overline{w}_2)_j^n = \frac{1}{2}\big((w_2)^+_{j-\frac{1}{2}} + (w_2)^-_{j+\frac{1}{2}}\big) \quad \text{and} \quad 2(\overline{q}_2)_j^n = \big((q_2)^+_{j-\frac{1}{2}} + (q_2)^-_{j+\frac{1}{2}}\big).$$

We now recall that our piecewise linear reconstruction procedure described in Section 3.3 ensures that all $(w_2)^{\pm}_{j\pm\frac{1}{2}} \geqslant 0$. Also, it follows from the formulas for the one-sided local speeds (3.22) that

$$a^+_{j\pm\frac{1}{2}} \geqslant 0, \quad a^-_{j\pm\frac{1}{2}} \leqslant 0, \quad 0 \leqslant \frac{\cos\theta_{j\pm\frac{1}{2}}(u_2)^-_{j\pm\frac{1}{2}} - a^-_{j\pm\frac{1}{2}}}{a^+_{j\pm\frac{1}{2}} - a^-_{j\pm\frac{1}{2}}} \leqslant 1, \quad 0 \leqslant \frac{a^+_{j\pm\frac{1}{2}} - \cos\theta_{j\pm\frac{1}{2}}(u_2)^+_{j\pm\frac{1}{2}}}{a^+_{j\pm\frac{1}{2}} - a^-_{j\pm\frac{1}{2}}} \leqslant 1.$$

Therefore, the last two terms on the right-hand side of (3.28) are nonnegative. The first two terms on the right-hand side of (3.28) will be nonnegative provided the CFL restriction

$$\lambda a(1+\delta) \leqslant 1/2, \quad a := \max_j\big\{\max\{a^+_{j+\frac{1}{2}}, -a^-_{j+\frac{1}{2}}\}\big\},\ \delta := \max_j\big\{\max\{\delta_j^+, \delta_j^-\}\big\}$$

is satisfied. This is only a slight modification of the usual CFL restriction $\lambda a \leqslant 1/2$ because δ will be very small in all practical applications. Hence, $(\overline{w}_2)_j^{n+1} \geqslant 0$ for all j, since these values are linear combinations of nonnegative point values of the reconstruction $\widetilde{w}_2$ with nonnegative coefficients.

Next, we show that the cell averages $(\overline{w}_1)_j^{n+1}$ remain nonnegative if they were nonnegative at the previous time step. According to (3.1) and (3.4), the first flux component $\mathbf{H}^{(1)}_{j+\frac{1}{2}}$ is given by

$$\begin{aligned}\mathbf{H}^{(1)}_{j+\frac{1}{2}} = {} & \frac{a^+_{j+\frac{1}{2}}\big((q_1)^-_{j+\frac{1}{2}} + (q_2)^-_{j+\frac{1}{2}}\big)(\cos\theta_{j+\frac{1}{2}})^3 - a^-_{j+\frac{1}{2}}\big((q_1)^+_{j+\frac{1}{2}} + (q_2)^+_{j+\frac{1}{2}}\big)(\cos\theta_{j+\frac{1}{2}})^3}{a^+_{j+\frac{1}{2}} - a^-_{j+\frac{1}{2}}} \\ & + \frac{a^+_{j+\frac{1}{2}}a^-_{j+\frac{1}{2}}}{a^+_{j+\frac{1}{2}} - a^-_{j+\frac{1}{2}}}\big[\varepsilon^+_{j+\frac{1}{2}} - \varepsilon^-_{j+\frac{1}{2}}\big],\end{aligned} \tag{3.29}$$

and according to (3.14) the source is given by

$$\overline{\mathbf{S}}^{(1)}_j = \overline{\mathbf{S}}^{(3)}_j + 2(\overline{q}_1)_j \cos\theta_{j+\frac{1}{2}}\cos\theta_{j-\frac{1}{2}}\frac{\cos\theta_{j+\frac{1}{2}} - \cos\theta_{j-\frac{1}{2}}}{\Delta x}. \tag{3.30}$$

Now taking into account that

$$\overline{\varepsilon}^n_j = (\overline{w}_1)^n_j + (\overline{w}_2)^n_j + B_j = \frac{1}{2}\big((w_1)^+_{j-\frac{1}{2}} + (w_1)^-_{j+\frac{1}{2}}\big) + \frac{1}{2}\big((w_2)^+_{j-\frac{1}{2}} + (w_1)^-_{j+\frac{1}{2}}\big) + B_j,$$

we use (3.11), (3.27), (3.29), and (3.30) to rewrite (3.24) as

$$\begin{aligned}\overline{\varepsilon}^{n+1}_j = {} & (\overline{w}_2)^{n+1} + B_j \\ & + \Big[\frac{1}{2} + \lambda\Big\{a^-_{j-\frac{1}{2}}\Big(\frac{a^+_{j-\frac{1}{2}} - \cos\theta_{j-\frac{1}{2}}(u_1)^+_{j-\frac{1}{2}}}{a^+_{j-\frac{1}{2}} - a^-_{j-\frac{1}{2}}}\Big) + \cos\theta_{j-\frac{1}{2}}(u_1)^+_{j-\frac{1}{2}}\delta^+_j\Big\}\Big](w_1)^+_{j-\frac{1}{2}} \\ & + \Big[\frac{1}{2} - \lambda\Big\{a^+_{j+\frac{1}{2}}\Big(\frac{\cos\theta_{j+\frac{1}{2}}(u_1)^-_{j+\frac{1}{2}} - a^-_{j+\frac{1}{2}}}{a^+_{j+\frac{1}{2}} - a^-_{j+\frac{1}{2}}}\Big) - \cos\theta_{j+\frac{1}{2}}(u_1)^-_{j+\frac{1}{2}}\delta^-_j\Big\}\Big](w_1)^-_{j+\frac{1}{2}} \\ & - \lambda a^-_{j+\frac{1}{2}}\Big(\frac{a^+_{j+\frac{1}{2}} - \cos\theta_{j+\frac{1}{2}}(u_1)^+_{j+\frac{1}{2}}}{a^+_{j+\frac{1}{2}} - a^-_{j+\frac{1}{2}}}\Big)(w_1)^+_{j+\frac{1}{2}} \\ & + \lambda a^+_{j-\frac{1}{2}}\Big(\frac{\cos\theta_{j-\frac{1}{2}}(u_1)^-_{j-\frac{1}{2}} - a^-_{j-\frac{1}{2}}}{a^+_{j-\frac{1}{2}} - a^-_{j-\frac{1}{2}}}\Big)(w_1)^-_{j-\frac{1}{2}},\end{aligned} \tag{3.31}$$

where $(\overline{w}_2)^{n+1}_j$ is defined by (3.28). Therefore, since $\overline{\varepsilon}^{n+1}_j = (\overline{w}_1)^{n+1} + (\overline{w}_2)^{n+1} + B_j$, we apply the same argument as for $(\overline{w}_2)^{n+1}_j$ and conclude that since $(\overline{w}_1)^{n+1}_j$ are linear combinations of nonnegative point values of the reconstruction $\widetilde{w}_1$ with nonnegative coefficients, $(\overline{w}_1)^{n+1}_j \geqslant 0$ for all j. □

Remark 3.2. Theorem 3.1 is still valid if one uses a higher-order SSP ODE solver because such solvers can be written as a convex combination of forward Euler steps (see [15] for details).

Remark 3.3. Implementing the friction stage of our operator splitting technique (outlined in Section 3.18) has no impact on the positivity preserving property of our scheme since neither ε nor w_2 is affected by (3.18)–(3.20).

4. Numerical Experiments

We have tested the proposed central-upwind scheme on a series of test problems. The first test problems in Section 4.1 demonstrate the well-balanced property of our scheme, the problems in Sections 4.2 and 4.3 demonstrate the good agreement between our scheme and that of [14], and the final example in Section 4.4 tests our scheme on a realistic scale. For all of the examples, we have set $r = 0.2$ (as was done in [14]), use the minmod parameter $\gamma = 1.3$, and impose free boundary conditions on both sides of the domain.

4.1. Small Perturbation of Steady State

We first demonstrate the well-balanced property of the scheme by considering a small perturbation of the "lake-at-rest" steady state on the domain $0 \leqslant x \leqslant 3$ with the bottom topography function and initial condition as follows:

$$B(x) = \begin{cases} 0.05(\cos(5\pi(x-1))+1)-2, & \text{if } 0.8 < x < 1.2, \\ -2, & \text{otherwise,} \end{cases} \tag{4.1}$$

$$(\varepsilon, q_1, w_2, q_2)(x,0) = \begin{cases} (0,0,\eta_2(x),0), & \text{if } 0.9 < x < 0.95, \\ (\eta_1,0,0,0), & \text{if } 2 < x < 2.1, \\ (0,0,0,0), & \text{otherwise.} \end{cases} \tag{4.2}$$

We will first take $\eta_1 = 10^{-3}$ and $\eta_2(x) \equiv 0$, and then take $\eta_1 = 0$ and $\eta_2(x) = -1.9 - B(x)$ (so that $w_2 + B \equiv -1.9$, a flat perturbation on a sloped bottom). These data are depicted in Figure 4.

In this example, we take $g = 1$ and $\delta_0 = 25°$. We compare our new well-balanced scheme applied to the reformulated system (2.2) to a scheme applied to the original system (1.1) in which the central-upwind fluxes are used to discretize the convection term on the left and all of the terms on the right-hand side are discretized in a straightforward manner using the midpoint rule (we will call this the "non-well-balanced scheme").

Figure 5 shows how the small perturbation in the water surface initially located near $x = 2$ splits into two waves moving in opposite directions. With the non-well-balanced scheme, some small surface waves are generated over the hump in the bottom and then they propagate in both directions. The left moving wave from the perturbation reaches the hump on the bottom at approximately $t = 0.6$, resulting in some small reflected waves moving to the right. These waves are slightly larger for the non-well-balanced scheme than for our new scheme. At the end of the simulation, both schemes have reached steady state, but the waves over the hump in the bottom persist for the non-well-balanced scheme, resulting in a steady state that is nonphysical.

Figure 6 shows how the perturbation in the lower layer initially located near $x = 1$ creates surface waves. At $t = 0.2$, the non-well-balanced scheme has already produced oscillations at the wave fronts as well as over the hump on the bottom. By the end of the simulation, the non-well-balanced scheme has again reached a nonphysical steady state.

In both of these small perturbation test problems, as the mesh is refined, the solution computed by the non-well-balanced scheme approaches the physical solution that is captured by our new well-balanced scheme applied to the reformulated system (2.2) on a coarse grid.

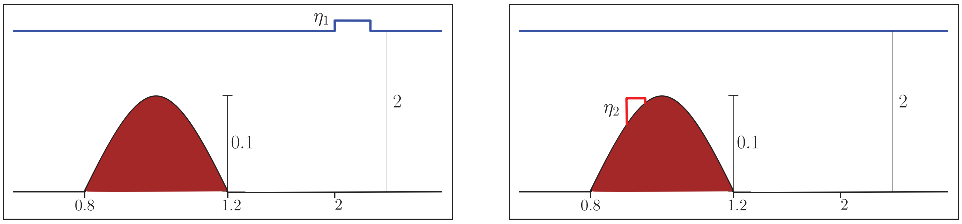

Figure 4. Initial data for small perturbation test problems as described by (4.1) and (4.2). For the solutions shown in Figures 5 and 6, $\eta_1 = 10^{-3}$ and $0.014 \leqslant \eta_2 \leqslant 0.05$, so these pictures are not to scale.

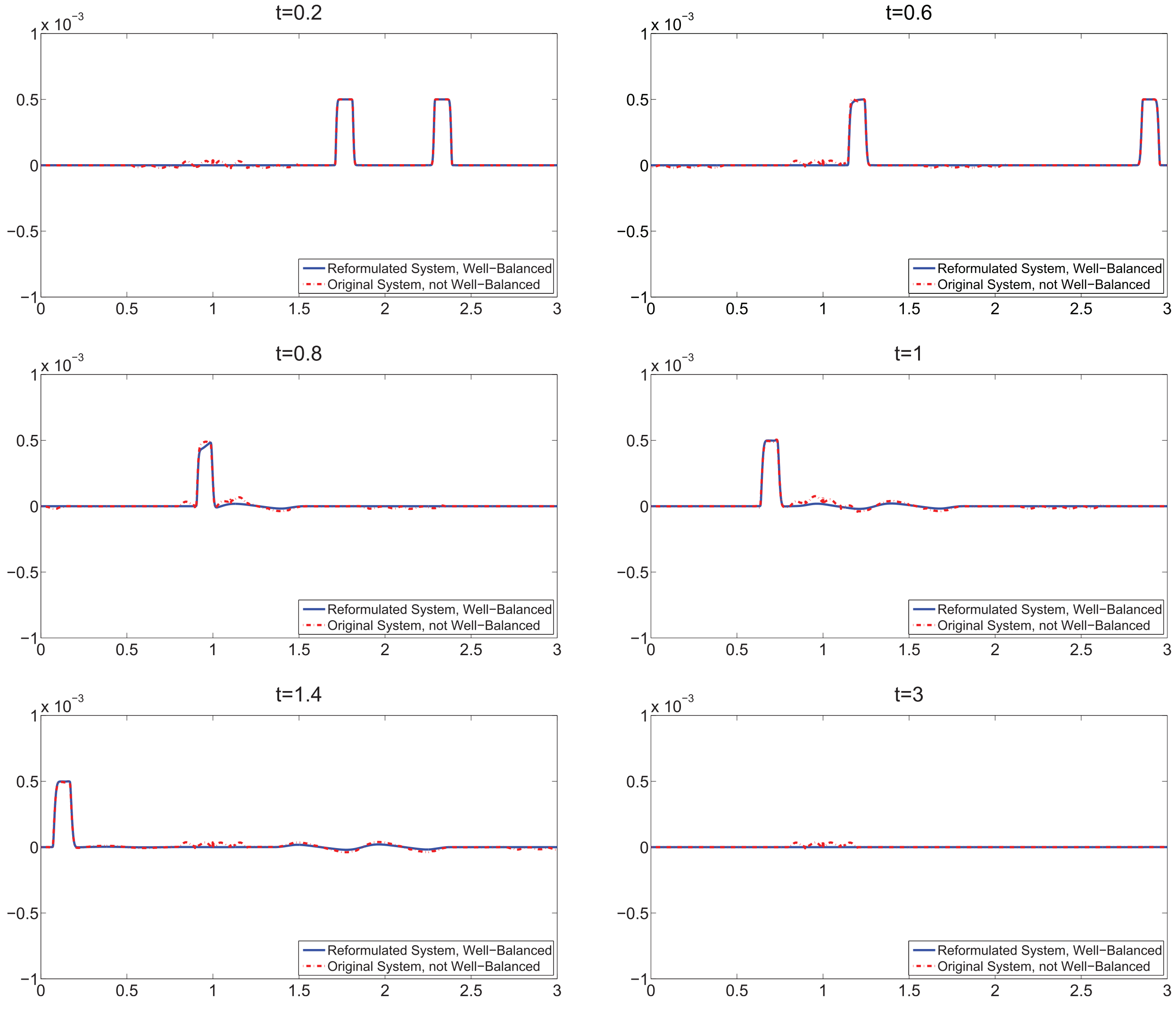

Figure 5. Solutions (the water surface) of (1.1) using the non-well-balanced scheme and of (2.2) using our well-balanced scheme with the same bottom topography and initial data given by (4.1) and (4.2) with $\eta_1 = 10^{-3}$ and $\eta_2 \equiv 0$; $\Delta x = 1/800$. The well-balanced scheme is oscillation-free and results in a physically relevant steady state whereas the non-well-balanced scheme develops nonphysical oscillations.

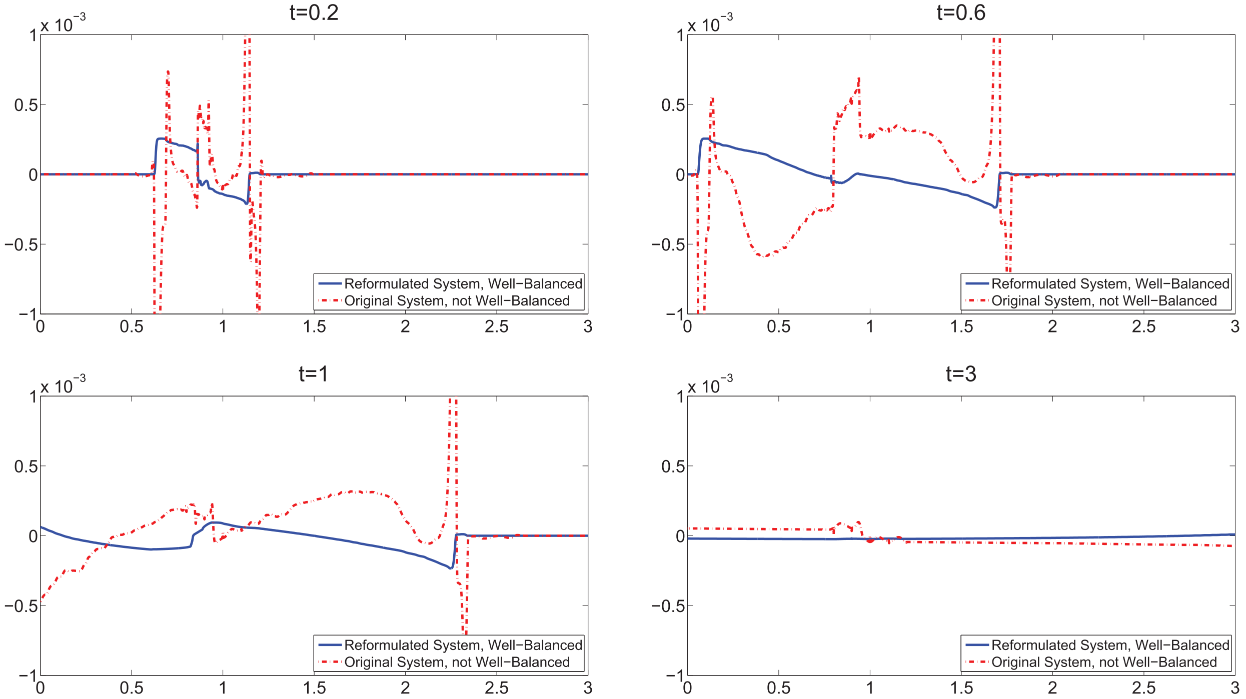

Figure 6. Solution (the water surface) of (1.1) using a non-well-balanced scheme and of (2.2) using our well-balanced scheme with the same bottom topography and initial data given by (4.1) and (4.2) with $\eta_1 \equiv 0$ and $\eta_2 - 1.9 - B(x)$; $\Delta x = 1/800$. Even though the well-balanced scheme develops small oscillations, it results in a physically relevant steady state whereas the non-well-balanced scheme produces physically irrelevant solution.

4.2. Surface Wave Generation

We next consider the first example from [14] which simulates a submarine landslide in a rectangular channel of length 10 m. The bottom B and the initial data are given by

$$B(x) = 0.2x - 2.7, \tag{4.3}$$

$$(\varepsilon, q_1, w_2, q_2)(x, 0) = \begin{cases} (0, 0, \cos(\arctan(0.2)), 0), & \text{if } 7 < x < 8, \\ (0, 0, 0, 0), & \text{otherwise.} \end{cases} \tag{4.4}$$

We take $g = 9.81$ and the Coloumb friction angle $\delta_0 = 25°$ as in [14]. The results of the simulation are shown in Figure 7. The sediment layer spreads out and slides down the hill, creating surface waves that travel in both directions and deform together with the bottom topography. The results are in good agreement with those reported in [14].

In Figure 8, we show the interface between the upper and lower layers at time $t = 5$, by which the mass has stopped sliding down the hill. Table 1 shows the errors and convergence rates of these solutions when comparing to the reference solution, which was computed with $\Delta x = 10/12800$.

4.3. Large-Scale Wave Generation

We next consider the third example from [14] in which more physically relevant initial data is considered in that the length scales are much greater. We consider a 30 km long domain

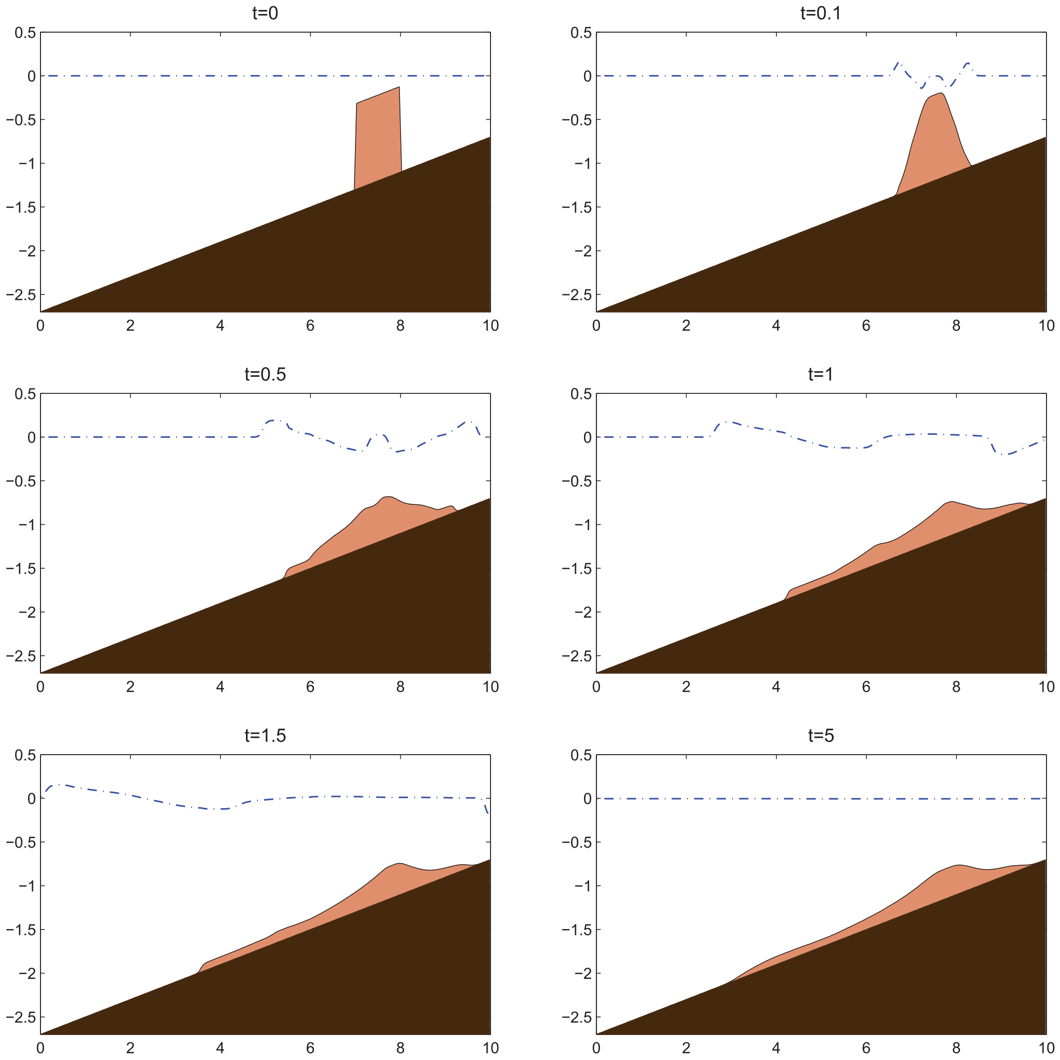

Figure 7. Time snapshots of the solution (the water surface, sediment layer, and bottom) of (2.2), (4.3), (4.4) with $\Delta x = 0.05$. The deformation due to gravity in the lower layer creates large waves on the water surface. The lower layer slides downhill and stops due to friction between the material and the non-erodible bottom B.

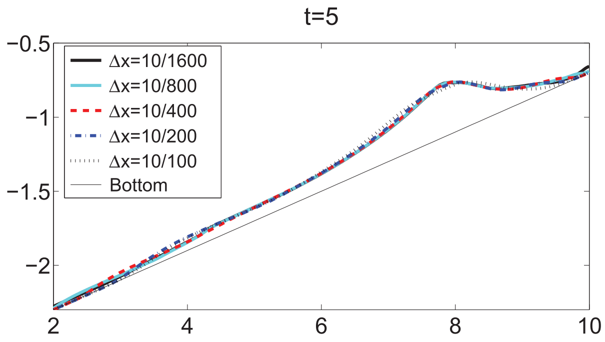

Figure 8. Zoom of the interface between the upper and lower layers at $t = 5.0$.

Δx	L^1-Error	Rate
10/100	0.1581	—
10/200	0.1116	0.46
10/400	0.0781	0.57
10/800	0.0502	0.64
10/1600	0.0338	0.57
10/3200	0.0222	0.61

Table 1. Errors and convergence rates of the lower layer in Section 4.2 at time $t = 5$ using $\Delta x = 10/12800$ to compute the reference solution.

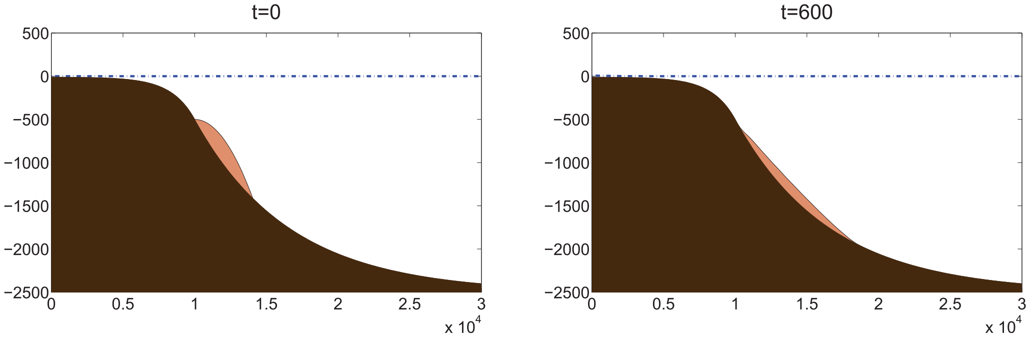

Figure 9. Initial condition and solution at $t = 600$. The lower layer slides down the hill and stops due to the friction between the lower layer and non-erodible bottom B. Surface waves cannot be seen at this zoom level.

with a depth on the order of 1 km. For this simulation we take $g = 9.81$ and $\delta_0 = 12°$ with the following bottom topography and initial condition:

$$B(x) = \begin{cases} -10 - 490\, e^{-6.1429\,(1-x/10000)}, & \text{if } x \leqslant 10000, \\ -2500 + 2000\, e^{-1.5050\,(x/10000-1)}, & \text{if } x > 10000, \end{cases} \tag{4.5}$$

$$(\varepsilon, q_1, w_2, q_2)(x, 0) = \big(0, 0, \max\{-B(x) - 1.8 \cdot 10^{-4}(x - 10000)^2, 0\}, 0\big). \tag{4.6}$$

The results obtained by our scheme with $\Delta x = 30000/500 = 60$ are similar to those in [14]. As Figure 9 shows, the lower layer slides down the hill and stops due to the friction between the lower layer and the bottom. Surface waves that are small relative to the size of the domain cannot be seen in Figure 9, but they have been captured and are shown in Figure 10.

4.4. Tsunami-Like Wave Generation

We next consider a situation in which a steep ridge on the bottom of the water body breaks off, causing a submarine landslide. For this simulation we take $g = 9.81$ and $\delta_0 = 35°$. The bottom topography is given by

$$B(x) = -\frac{3}{4} - \frac{1}{2}\big[1 - (2 - x) - \mathrm{sgn}(2 - x)\big(1 - (|2 - x|^c + 1)^{1/c}\big)\big], \tag{4.7}$$

which essentially describes two piecewise constant pieces for $x < 1$ and $x > 3$ connected by a linear piece where the corners are smoothed out (the smoothing parameter is taken to be

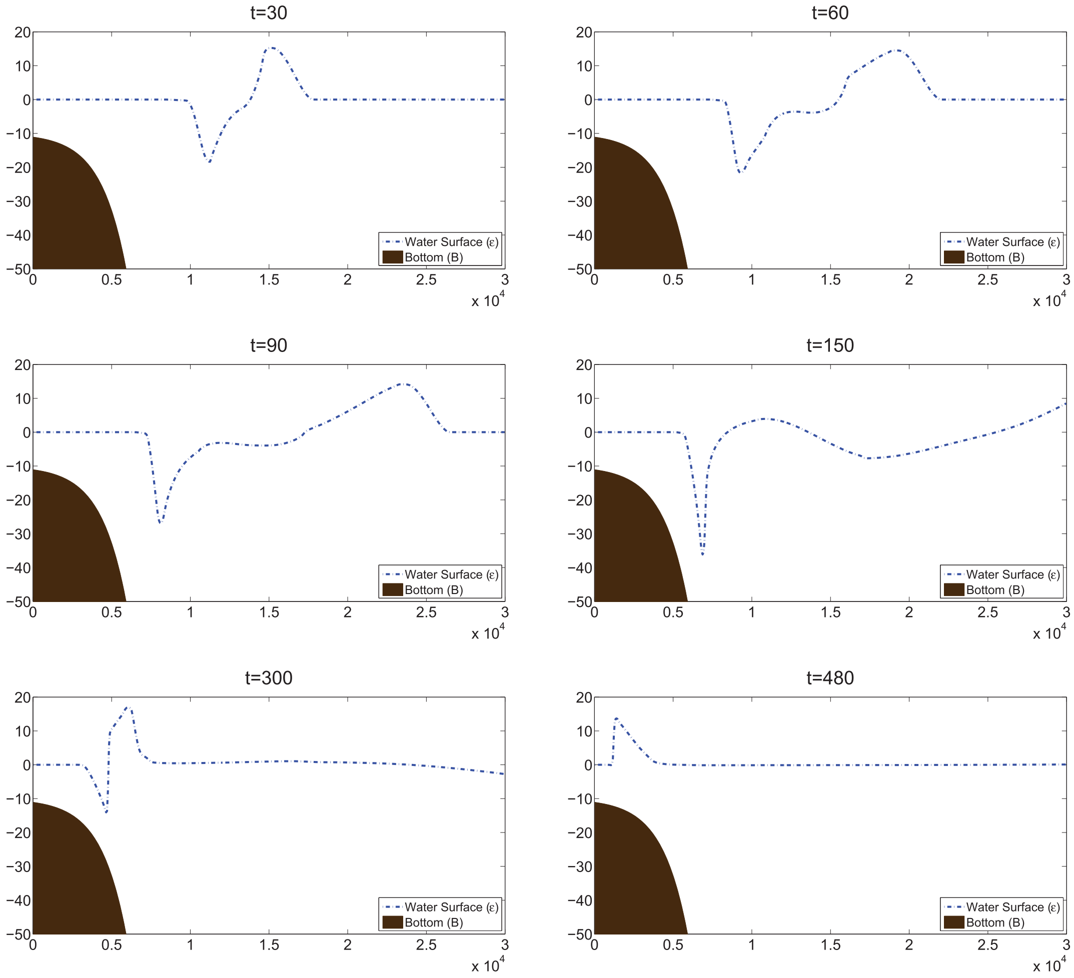
t=30

t=60

t=90

t=150

t=300

t=480

Figure 10. Zoomed time snapshots of the solution of (2.2) with the initial condition and bottom function given by (4.6) and (4.5), respectively.

$c = 10$). The initial condition,

$$(\varepsilon, q_1, w_2, q_2)(x, 0) = \begin{cases} (0, 0, \max\{-1 - B(x), 0\}, 0), & \text{if } 0.5 < x < 3.5, \\ (0, 0, 0, 0), & \text{otherwise,} \end{cases} \tag{4.8}$$

together with the bottom structure (4.7) are shown in Figure 11.

Figure 12 shows how submarine landslide creates surface waves propagating in each direction. The left-moving wave leaves the domain by $t = 5.0$ while the right-moving wave moves over the flat bottom in the characteristic tsunami wave shape. We are able to capture the surface dynamics even though the waves are small relative to the total water depth. Figure 13 depicts the propagation of this wave over a flat bottom for a long distance. One can see that the wave is dissipating, suggesting that this model is insufficient for studying long-time propagation of tsunami-like waves. It is known that tsunami-like waves do not dissipate and preserve their initial shapes in dispersive models like the Green–Naghdi equations [16] and their modern counterparts (see, e.g., [2–4, 6, 7] and references therein). We therefore believe that a plausible approach to modeling tsunami waves generated by submarine landslides should be the following one: Use the system (2.2) for modeling the initial stage of the wave formation and then switch to a dispersive shallow water system to model the long-time propagation of the generated tsunami-waves.

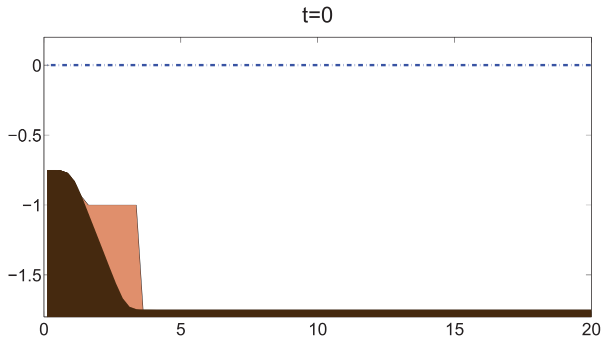

Figure 11. Bottom topography and initial condition given by (4.7) and (4.8), respectively. There is a small ridge formed by the sediment layer that deforms and generates small surface waves.

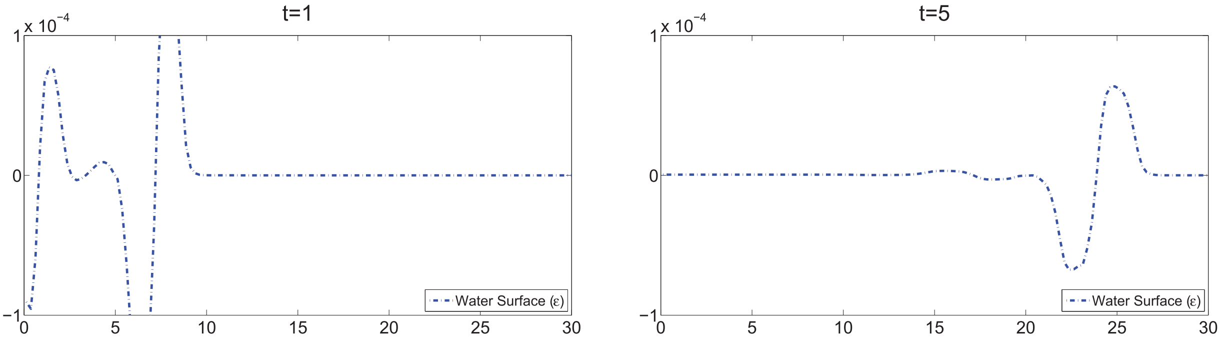

Figure 12. Solution (the water surface) of tsunami-like wave generation simulation at different time levels. The relatively small submarine landslide creates very small surface waves that are undetectable when zoomed out. Our new scheme is able to capture the very small wave with characteristic tsunami shape. The solution is computed on a computational domain $0 < x < 100$ using $\Delta x = 0.25$ (the plots are zoomed to $0 \leqslant x \leqslant 30$).

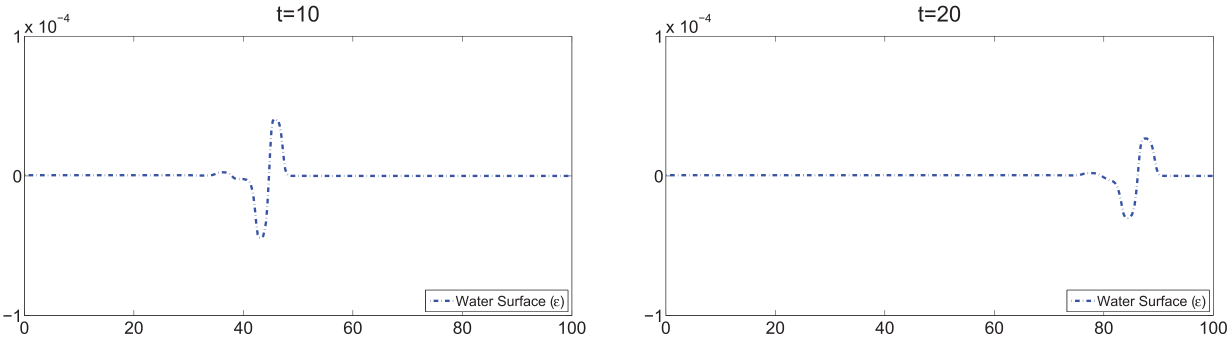

Figure 13. The same simulation as in Figure 12, but shown on a larger domain and at later times.

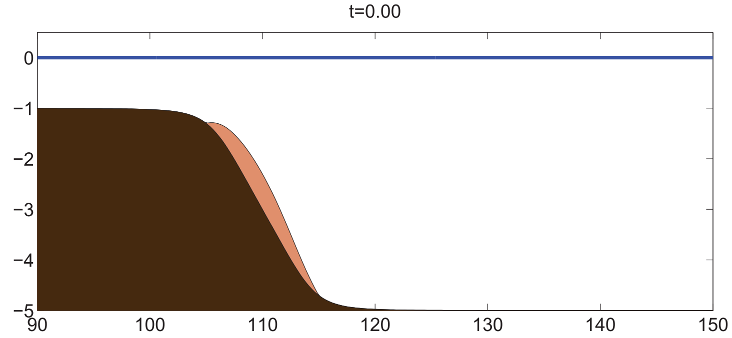

Figure 14. Bottom topography and initial condition given by (4.9) and (4.10), respectively. There is a small ridge formed by the sediment layer that deforms and generates small surface waves.

4.5. Large-Scale Tsunami-Like Wave Generation

We again consider a situation in which a ridge on the bottom of the water body breaks off, causing a submarine landslide. The domain is the interval $[0, 500]$ and we take $\delta_0 = 12°$. In order to consider this on a large spatial scale (km), we take $g = 271008$ km/hr^2. The bottom topography is given by

$$B(x) = -1 - 2\Big[1 - \frac{2(110-x)}{10} - \operatorname{sign}(110-x)\Big(1 - \Big(1 + \Big|\frac{2(110-x)}{10}\Big|^c\Big)^{\frac{1}{c}}\Big)\Big], \tag{4.9}$$

which essentially describes two piecewise constant pieces for $x < 105$ and $x > 115$ connected by a linear piece where the corners are smoothed out (the smoothing parameter is again taken to be $c = 10$). The initial condition,

$$(\varepsilon, q_1, w_2, q_2)(x, 0) = \begin{cases} (0, 0, 0.7\sin((x-105)\pi/10), 0), & \text{if } 105 < x < 115, \\ (0, 0, 0, 0), & \text{otherwise,} \end{cases} \tag{4.10}$$

together with the bottom structure (4.7) are shown in Figure 11.

Figure 15 shows how submarine landslide creates surface waves propagating in each direction. The left-moving wave leaves the domain by $t = 0.4$ while the right-moving wave moves over the flat bottom in the characteristic tsunami wave shape, size, and speed. We are able to capture the surface dynamics even though the waves are small relative to the total water depth.

References

[1] R. Abgrall and S. Karni, *Two-layer shallow water system: A relaxation approach*, SIAM J. Sci. Comput., **31** (2009), pp. 1603–1627.

[2] E. Barthelemy, *Nonlinear shallow water theories for coastal waves*, Surv. Geophys., **25** (2004), pp. 315–337.

[3] J. L. Bona, M. Chen, and J.-C. Saut, *Boussinesq equations and other systems for small-amplitude long waves in nonlinear dispersive media. I. Derivation and linear theory*, J. Nonlinear Sci., **12** (2002), pp. 283–318.

[4] J. L. Bona, M. Chen, and J.-C. Saut, *Boussinesq equations and other systems for small-amplitude long waves in nonlinear dispersive media. II. The nonlinear theory*, Nonlinearity, **17** (2004), pp. 925–952.

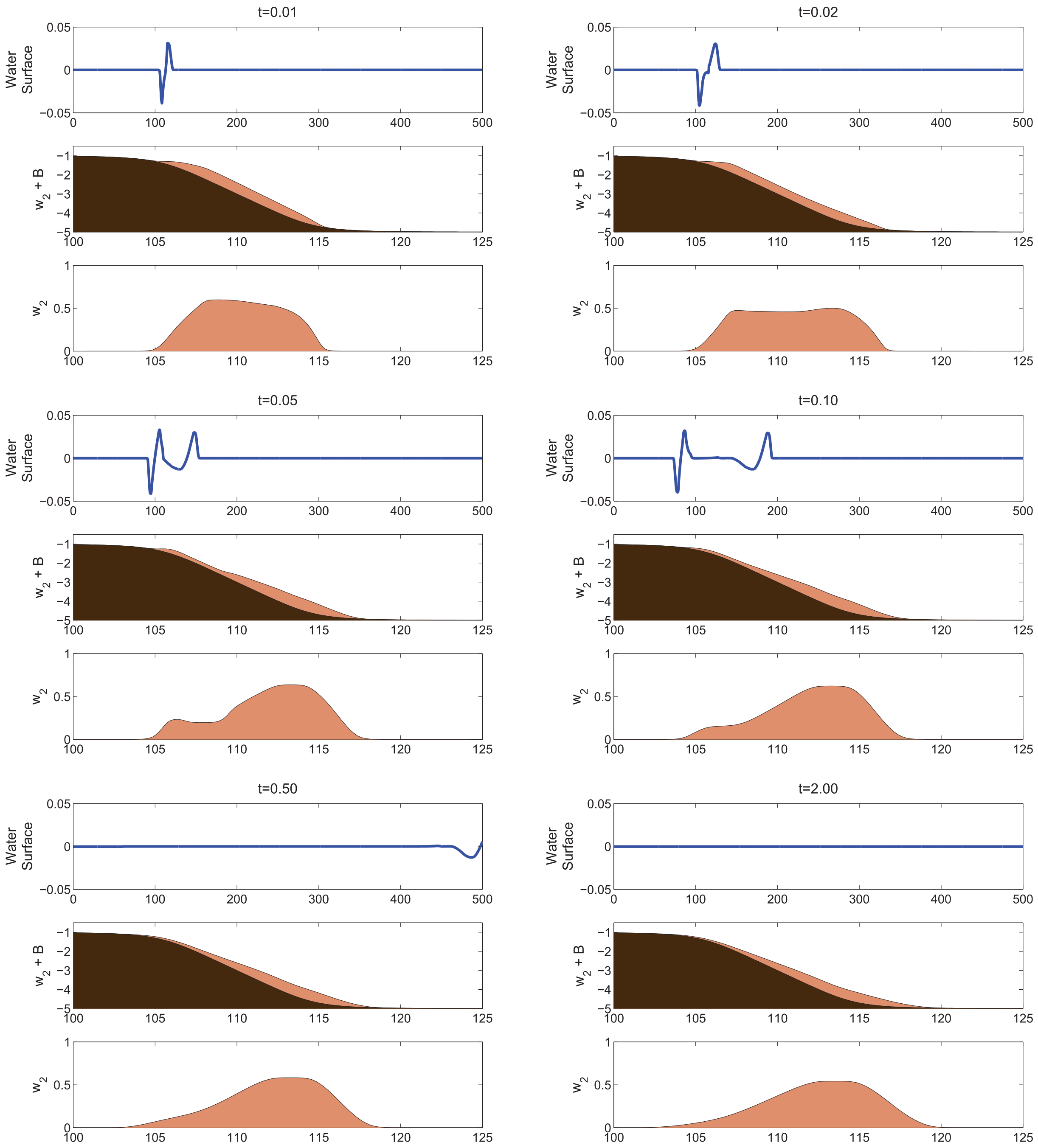

Figure 15. Solution (the water surface, the lower layer atop the bottom, and just the lower layer) of tsunami-like wave generation simulation at different time levels. The submarine landslide creates small surface waves that are undetectable when zoomed out. Our new scheme is able to capture the small wave with characteristic tsunami shape. The solution is computed on a computational domain $0 < x < 500$ using $\Delta x = 0.25$ (the plots of the lower layer are zoomed to $100 \leqslant x \leqslant 125$).

[5] F. Bouchut and T. Morales de Luna, *An entropy satisfying scheme for two-layer shallow water equations with uncoupled treatment*, M2AN Math. Model. Numer. Anal., **42** (2008), pp. 683–698.

[6] M.-O. Bristeau, N. Goutal, and J. Sainte-Marie, *Numerical simulations of a non-hydrostatic shallow water model*, Comput. Fluids, **47** (2011), pp. 51–64.

[7] M.-O. Bristeau and J. Sainte-Marie, *Derivation of a non-hydrostatic shallow water model; comparison with Saint-Venant and Boussinesq systems*, Discrete Contin. Dyn. Syst. Ser. B, **10** (2008), pp. 733–759.

[8] S. Bryson, Y. Epshteyn, A. Kurganov, and G. Petrova, *Well-balanced positivity preserving central-upwind scheme on triangular grids for the Saint-Venant system*, M2AN Math. Model. Numer. Anal., **45** (2011), pp. 423–446.

[9] M. J. Castro, P. G. LeFloch, M. L. Muñoz-Ruiz, and C. Parés, *Why many theories of shock waves are necessary: Convergence error in formally path-consistent schemes*, J. Comput. Phys., **227** (2008), pp. 8107–8129.

[10] M. Castro, J. Macías, and C. Parés, *A Q-scheme for a class of systems of coupled conservation laws with source term. Application to a two-layer 1-D shallow water system*, M2AN Math. Model. Numer. Anal., **35** (2001), pp. 107–127.

[11] M. J. Castro, J. Macías, C. Parés, J. A. García-Rodríguez, and E. Vázquez-Cendón, *A two-layer finite volume model for flows through channels with irregular geometry: Computation of maximal exchange solutions. Application to the Strait of Gibraltar*, Commun. Nonlinear Sci. Numer. Simul., **9** (2004), pp. 241–249.

[12] M. J. Castro Díaz, T. Chacón Rebollo, E. D. Fernández-Nieto, and C. Pares, *On well-balanced finite volume methods for nonconservative nonhomogeneous hyperbolic systems*, SIAM J. Sci. Comput., **29** (2007), pp. 1093–1126.

[13] F. Enet, S. T. Grilli, and P. Watts, *Laboratory experiments for tsunamis generated by underwater landslides: Comparison with numerical modeling*, in: Proceedings of the 13th Offshore and Polar Engineering Conference, International Society of Offshore and Polar Engineers, Cupertino, 2003, pp. 372–379.

[14] E. D. Fernández-Nieto, F. Bouchut, D. Bresch, M. J. Castro Díaz, and A. Mangeney, *A new Savage–Hutter type model for submarine avalanches and generated tsunami*, J.Comput. Phys., **227** (2008), pp. 7720–7754.

[15] S. Gottlieb, C.-W. Shu, and E. Tadmor, *Strong stability-preserving high-order time discretization methods*, SIAM Rev., **43** (2001), pp. 89–112.

[16] A. E. Green and P. M. Naghdi, *A derivation of equations for wave propagation in water at variable depth*, J. Fluid Mech., **78** (1976), pp. 237–246.

[17] S. T. Grilli and P. Watts, *Tsunami generation by submarine mass failure. I: Modeling, experimental validation, and sensitivity analyses*, J. Waterway Port Coastal Ocean Eng., **131** (2005), pp. 283–297.

[18] P. Heinrich, *Nonlinear water waves generated by submarine and areal landslides*, J. Waterway Port Coastal Ocean Eng., **118** (1992), pp. 249–266.

[19] P. Heinrich, A. Piatanesi, and H. Hebert, *Numerical modelling of tsunami generation and propagation from submarine slumps: The 1998 Papua New Guinea event*, Geophys. J. Int., **145** (2001), pp. 97–111.

[20] A. Kurganov and D. Levy, *Central-upwind schemes for the Saint-Venant system*, M2AN Math. Model. Numer. Anal., **36** (2002), pp. 397–425.

[21] A. Kurganov and C.-T. Lin, *On the reduction of numerical dissipation in central-upwind schemes*, Commun. Comput. Phys., **2** (2007), pp. 141–163.

[22] A. Kurganov, S. Noelle, and G. Petrova, *Semi-discrete central-upwind scheme for hyperbolic conservation laws and Hamilton–Jacobi equations*, SIAM J. Sci. Comput., **23** (2001), pp. 707–740.

[23] A. Kurganov and G. Petrova, *A second-order well-balanced positivity preserving central-upwind scheme for the Saint-Venant system*, Commun. Math. Sci., **5** (2007), pp. 133–160.

[24] A. Kurganov and G. Petrova, *A central-upwind scheme for nonlinear water waves generated by submarine landslides*, in: Hyperbolic Problems: Theory, Numerics, Applications (Lyon 2006), Springer, 2008, pp. 635–642.

[25] A. Kurganov and G. Petrova, *Central-upwind schemes for two-layer shallow equations*, SIAM J. Sci. Comput., **31** (2009), pp. 1742–1773.

[26] A. Kurganov and E. Tadmor, *New high resolution central schemes for nonlinear conservation laws and convection-diffusion equations*, J. Comput. Phys., **160** (2000), pp. 241–282.

[27] K.-A. Lie and S. Noelle, *On the artificial compression method for second-order nonoscillatory central difference schemes for systems of conservation laws*, SIAM J. Sci. Comput., **24** (2003), pp. 1157–1174.

[28] J. Macías, C. Pares, and M. J. Castro, *Improvement and generalization of a finite element shallow-water solver to multi-layer systems*, Internat. J. Numer. Methods Fluids, **31** (1999), pp. 1037–1059.

[29] A. Mangeney-Castelnau, J. P. Vilotte, M. O. Bristeau, B. Perthame, F. Bouchut, C. Simeoni, and S. Yernini, *Numerical modeling of avalanches based on Saint Venant equations using a kinetic scheme*, J. Geophys. Res., **108** (2003), p. 2527.

[30] M. Mignotte and D. Stefanescu, *On an estimation of polynomial roots by Lagrange*, Technical report 025/2002, pp. 1–17, IRMA Strasbourg, 2002, `http://hal.archives-ouvertes.fr/hal-00129675/en/`.

[31] H. Nessyahu and E. Tadmor, *Nonoscillatory central differencing for hyperbolic conservation laws*, J. Comput. Phys., **87** (1990), pp. 408–463.

[32] M. Ortiz, E. Gomez-Reyes, and H. Velez-Munoz, *A fast preliminary estimation model for transoceanic tsunami propagation*, Geofísica Internacional, **39** (2000), pp. 207–220.

[33] P. K. Sweby, *High resolution schemes using flux limiters for hyperbolic conservation laws*, SIAM J. Numer. Anal., **21** (1984), pp. 995–1011.

[34] P. Watts, *Wavemaker curves for tsunamis generated by underwater landslides*, J. Waterway Port Coastal Ocean Eng., **124** (1998), pp. 127–137.

[35] P. Watts, *Tsunami features of solid block underwater landslides*, J. Waterway Port Coastal Ocean Eng., **126** (2000), pp. 144–152.